ACS Catalysis

pubs.acs.org/acscatalysis Research Article

Catalytic Methane Pyrolysis in Molten Alkali Chloride Salts Containing Iron

Dohyung Kang,[#] Clarke Palmer,[#] Davide Mannini, Nazanin Rahimi, Michael J. Gordon, Horia Metiu, and Eric W. McFarland*

Cite This: *ACS Catal.* 2020, 10, 7032−7042 Read Online

ACCESS | Metrics & More | Article Recommendations | Supporting Information

ABSTRACT: Mixtures of molten iron−sodium-potassium chloride salts are found to be catalytic for methane pyrolysis. In a differential bubble column reactor, the apparent activation energy of the molten salt decreases from 301 kJ/mol for the eutectic NaCl-KCl to 171 kJ/mol for 3 wt % of iron-added as $FeCl_3$. The solid carbon produced in the iron-containing salt mixture has a graphitic structure which is distinct from the more disordered carbon produced in the iron-free eutectic, suggesting a different solid carbon formation pathway. Results from H−D exchange investigations are consistent with a different reaction pathway for methane pyrolysis in the iron-containing NaCl-KCl melt than in the melt without Fe. The activity of the salt mixture was stable for over 50 h, producing molecular hydrogen and separable solid carbon. It is likely that the activity is due to the presence of Fe in molecular ions stabilized in the NaCl-KCl melt that facilitate the C−H bond activation in methane.

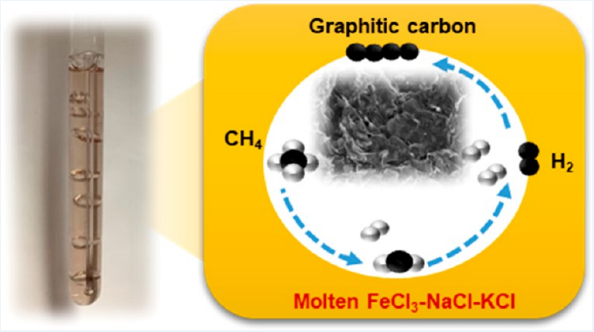

KEYWORDS: *methane decomposition, bubble column reactor, molten salt, hydrogen, iron chloride*

1. INTRODUCTION

Approximately 50 million tons of hydrogen are produced annually for use as a critical feedstock for producing chemicals and fuels. Today, most industrial hydrogen is produced by reforming methane and other hydrocarbons with steam ($CH_4 + 2H_2O \rightarrow 4H_2 + CO_2$), generating annually more than 300 million tons of CO_2. A cost-effective means of producing hydrogen without generating CO_2 would improve the sustainability of the chemical industry and make possible the future use of hydrogen as a CO_2-free fuel.[1−4]

Although renewable sources of hydrogen for use as a fuel have long been investigated, none have been cost competitive with steam methane reforming (SMR) in the absence of a tax or negative cost assigned to the produced CO_2. If minimization of CO_2 is a priority and economically incentivized, methane can also be decomposed into molecular hydrogen and solid carbon by "pyrolysis" ($CH_4 \rightarrow C + 2H_2$). Pyrolysis produces less hydrogen per methane molecule than SMR; however, the endothermic reaction (ΔH° = 37.5 kJ/mol H_2) requires approximately the same energy as SMR per unit H_2 produced (ΔH° = 41.3 kJ/mol H_2). Only if there were to be a cost associated with carbon dioxide generation and/or if the solid carbon produced could be economically removed from the reactor and had commercial value, then methane pyrolysis using abundant natural gas could be a cost-effective process for hydrogen production during the inevitable future transition to an energy economy independent of increasingly scarce fossil fuels.[5−7] Even if there is little demand for the coproduced carbon from pyrolysis, it can be stored for the long-term at far lower cost than sequestration of gas-phase CO_2.

Thermal decomposition of methane in the gas phase without a catalyst proceeds by way of homogeneous C−H bond cleavage and subsequent CH_3 radical generation at high temperatures. C_{2+} hydrocarbons are generated by the reaction between CH_3 radicals and other hydrocarbon intermediates.[8−10] Without a catalyst, at temperatures under 1100 °C, the reaction rates are slow and the selectivity to hydrogen is limited; there is relatively high selectivity to hydrocarbon intermediates such as ethylene, acetylene, and aromatics.[10−13] Methane pyrolysis on solid catalysts, such as Ni and other transition metals, has been widely studied.[14−16] On solid catalyst surfaces, methane can undergo rapid dissociative chemisorption and subsequent dehydrogenations and C−C bond formation with adjacent intermediates. Further oligomerization of carbon species on the solid catalyst eventually forms immobile coke which deactivates the surface of the solid catalyst.[17] To regenerate the activity of solid catalysts, the solid

Received: March 18, 2020
Revised: May 23, 2020
Published: June 1, 2020

https://dx.doi.org/10.1021/acscatal.0c01262
ACS Catal. 2020, 10, 7032−7042

carbon is gasified[18−21] by oxidation, which gives rise to undesirable CO_2 emission.

By reacting methane in high-temperature liquids, it has been shown that hydrogen can be produced together with solid carbon that is separable from the liquid. Methane pyrolysis on a catalytic gas−liquid interface in a bubble column reactor does not deactivate like solid catalysts because the active surface of the liquid is continuously renewed as the gas passes through the melt.[22] In a bubble column system, the produced solid carbon accumulates and is readily recovered by solid−liquid separations.

High-temperature molten metals and salts have been utilized for pyrolysis of biomass and hydrocarbons.[23,24] Several molten metal systems which are stable at the elevated temperature have been examined for methane pyrolysis.[25−30] Molten metal alloys of bismuth have been shown to be active catalysts for pyrolysis, including Bi−Ni[29] and Bi−Cu.[30] These molten alloys continuously produced separable carbon in the melt without deactivation. Molten salts have also been used for pyrolysis of C_{2+} hydrocarbons.[31,32] Less work has been done investigating molten salts for methane pyrolysis[33] because few salts are thought to be active and stable at the high temperatures required for the activation of the strong C−H bond in methane.

Simple alkali halide salts such as NaCl are stable under the high-temperature reducing conditions of methane pyrolysis; however, they are wide band gap insulating liquids with no significant activity for methane activation.[33,34] We have recently shown that addition of Mn salts to alkali halides gives rise to salt mixtures active for methane pyrolysis.[33] Mn(II) is thermodynamically stable in the presence of methane and hydrogen at high temperatures; however, many transition metal ions are not.[35,36] At approximately 50 mol % Mn(II) chloride in KCl, the tetrahedrally coordinated Lewis acidic $(MnCl_4)^-$ molecular ion is stabilized, which we speculated was responsible for the methane activation. Most common pure transition metal halide salts including those of Ni, Co, Cu, and Fe are known to possess Lewis acidity; however, they are readily reduced at high temperature in hydrogen or methane. Iron chlorides are generally expected to be reduced to Fe^0 at high temperatures in the presence of hydrogen and/or methane. In mixtures of alkali chloride salts, many Lewis acid metal halide salts including Fe(III) chloride are known to form more stable molecular ion coordination complexes.[37−39] In particular, tetrahedrally coordinated $(FeCl_4)^-$ was identified in mixed Group IA alkali chlorides.[40]

We investigated the reactivity for methane pyrolysis and stability of iron in mixtures of sodium chloride (NaCl) and potassium chloride (KCl), where we anticipate molecular ions including $(FeCl_4)^-$ will be formed. Whereas the eutectic NaCl-KCl melt is a poor catalyst for methane pyrolysis, we observe that mixtures of iron(III) chloride ($FeCl_3$), NaCl, and KCl formed stable molten salts at high temperature that have high activity for pyrolysis. There have been few works exploring the stability and catalytic functionality of $FeCl_3$ and its molecular ions in salt mixtures at elevated temperature (>600 °C). Iron chloride salts have a relatively low toxicity and can be obtained in large quantities at lower costs than other melts which have been reported as molten catalysts for methane pyrolysis.[29,33] The following questions are addressed in this Article: (1) What are the kinetic parameters for methane pyrolysis in a bubble column reactor with molten NaCl-KCl and how do they change with increasing Fe content? (2) Is the activity for pyrolysis in the melt mixture stable? (3) What is the reaction mechanism for methane pyrolysis in the iron-containing melts? (4) What are properties of the solid carbon product produced in the iron-containing melt mixture?

2. EXPERIMENTAL SECTION

2.1. Preparation of Iron-Containing Eutectic NaCl-KCl Melts. Several salt mixtures were prepared from iron(III) chloride hexahydrate ($FeCl_3{\cdot}6H_2O$, Sigma-Aldrich, ≥ 99.8%), sodium chloride (NaCl, Sigma-Aldrich, ≥ 99.0%), and potassium chloride (KCl, Sigma-Aldrich, ≥ 99.0%). The molar ratio of NaCl to KCl was fixed at the eutectic: 1.02, which is labeled as NaKCl. $FeCl_3{\cdot}6H_2O$ was added such that the final iron weight percentages were 1%, 3%, 5%, and 7%. The solid salts were mechanically mixed and then dehydrated under Ar flow at 110 °C for a minimum of 24 h. For melting the salts, the temperature was increased slowly (less than 0.2 °C/min) until the mixture was melted, approximately 660 °C. After melting, the molten salt was sparged with hydrogen 10% vol in argon for 12 h. As prepared, the molten salts were transparent, with a brownish color visible with increasing iron content.

2.2. Methane Pyrolysis Kinetics in a Differential Molten Salt Bubble Column. The experimental setup to measure activity and kinetic parameters of molten salts in a bubble column has been described previously (Figure 1).[33] In

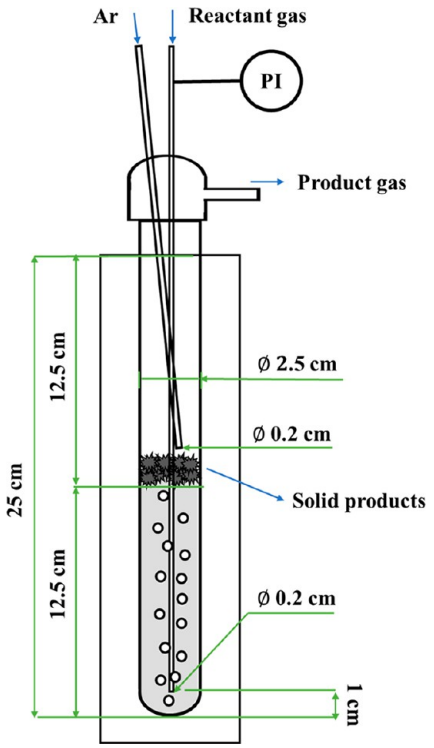

Figure 1. Experimental setup for a bubble column reactor system.

bubble columns at relatively low inlet flow rates and short residence times, pyrolysis can be assumed to occur isothermally and isobarically in individual noncoalescing bubbles modeled as a constant pressure batch reactor with an approximately constant surface to volume ratio. The quartz tube reactor with a 2.5 cm inside diameter was filled to 12.5 cm (61.3 mL) with the molten salt and mounted in a furnace such that a 25 cm length was heated and maintained at constant

https://dx.doi.org/10.1021/acscatal.0c01262
ACS Catal. 2020, 10, 7032−7042

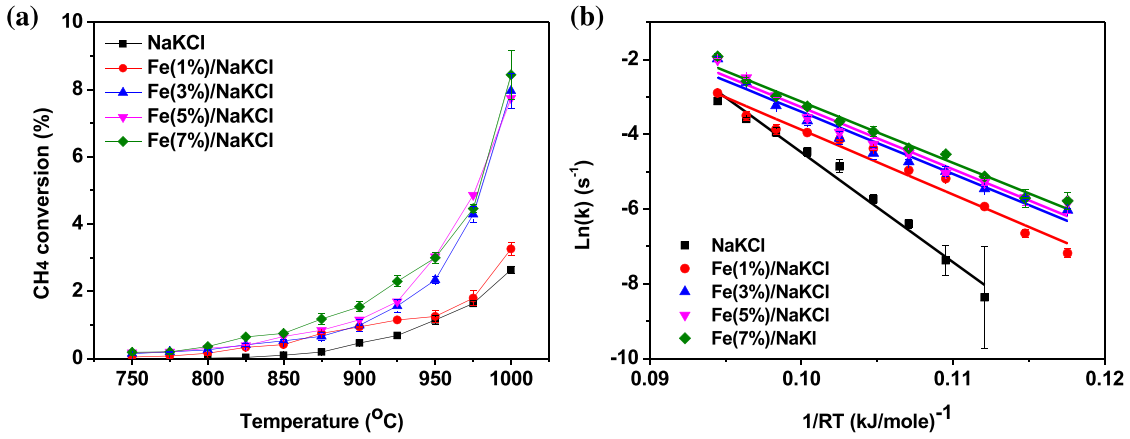

Figure 2. Catalytic activity of Fe/NaKCls for methane pyrolysis: 20 sccm of reactant gas (CH_4:Ar = 50:50 vol %) and 50 sccm of sweep gas (100 vol % of Ar). (a) Methane conversion versus temperature. (b) Arrhenius plots for methane consumption rate measured in differential reactor.

temperature. The reactant gas mixture was injected into the melt through a quartz capillary tube (i.d. = 0.2 cm) open 1 cm from the bottom of the melt. The bubble residence time in the melt was approximately 0.5 s with the bubble rise velocity of ~23 cm/sec. Under these conditions at low methane conversions, the relationship between the apparent first-order reaction rate constant and the conversion in the bubble column is given by $X \approx k\tau$. From the conversion and the known residence time, the rate constant is determined. From an Arrhenius plot of conversions measured at several different temperatures, an apparent activation energy and pre-exponential factor can be determined.

Density and surface tension measurements were calculated using the maximum bubbling pressure method. Time-dependent pressure traces of the inlet gas passing through the injector tube were measured for different depths into the melt. Custom-made, tapered 1/4 in. quartz injector tubes with inner tip diameters of ~1.5 mm were used for these measurements (see Figure S1 in SI). The total pressure is expressed as a combination of the hydrostatic pressure and the surface tension forces according to the Young−Laplace equation:

$$P(t) = P_{atm} + \rho g d + \frac{2\sigma}{R(t)}$$

The total pressure is inversely proportional with the radius of curvature of the bubble (R). Therefore, the total pressure reaches a maximum pressure, P_{MAX}, when the radius of curvature is minimized (i.e., when the radius of curvature is equal to the radius of the injector tube, R_{TUBE}):

$$P_{MAX} = P_{atm} + \rho g d + \frac{2\sigma}{R_{TUBE}}$$

The maximum pressure at each depth (d) is plotted versus depth (Figure S1d) on a linear scale. The surface tension (σ) is calculated from the y-intercept, as the atmospheric pressure (P_{atm}) and injector tube radius are known. The density (ρ) is calculated from the slope, as the gravitational constant (g) is known.

In situ bubble sizes were estimated from the periodicity of the same pressure trace used for the above measurements. The frequency of the bubble generation was determined, and the volume of the bubbles was calculated using the known volumetric flow rate of the inlet gas.

The empty space of the reactor above the melt surface was swept with 50 sccm of inert Ar gas to minimize any gas-phase reactions in the headspace. The gas mixtures leaving the reactor were analyzed using a HP 5890 Series II gas chromatograph equipped with 5 Å molecular sieve packed column. The deuterated methane products from hydrogen−deuterium exchange in mixtures of CH_4 and D_2 was monitored using a residual gas analyzer mass spectrometer (Stanford Research Systems, RGA 200).

Because the bubble rise velocity is a function of the bubble size, it is approximately constant at various flow rates.[33] The bubble size was estimated from the pressure measurement of the capillary quartz tube where the reactant gas is introduced (Figure S2). The diameter of the bubble in Fe(3%)/NaKCl is approximately 10% smaller than that in NaKCl because of the marginally higher density and lower surface tension of Fe(3%)/NaKCl. The bubble size increases slightly with increasing bubbling gas flow rate in all melts studied. The variation in bubble size at a given flow rate does not change significantly with different flow rates in any of the melts studied (less than 10% of standard deviation).

The gas flow rate for measurements of activity was selected. There are two stages for reaction in the melt: (1) during bubble formation at the tip of the capillary tube and (2) during the bubble rise through the melt. The time required to grow a bubble depends on the gas flow rate. However, once the bubble forms and detaches at the tip of the tube, the bubble rises at a constant velocity independent of flow rate until the gas holdup exceeds 5−10%. At very slow flow rates, the bubble growth at the tube tip is longer than its rise time in the column, and methane conversion can be significant. Therefore, a relatively high flow rate is used to ensure methane conversion occurs predominately in the rising bubble with the bubble growth time negligible compared with the bubble rise time (Figure S3).

2.3. Salt and Carbon Characterization. In situ analysis of the molten salt is difficult at the operating temperature of 1000 °C and beyond the scope of our current investigations. Therefore, structural characteristics of the molten salt were inferred from the solid salt after rapidly quenching the melt. Using a small diameter (~1 cm) quartz tube to facilitate the heat transfer, the hot molten salt was rapidly cooled in liquid nitrogen under flowing Ar. The resultant solid salt was

https://dx.doi.org/10.1021/acscatal.0c01262
ACS Catal. 2020, 10, 7032−7042

collected and maintained under Ar to prevent the adsorption of water prior to spectroscopic characterization.

The solid carbon formed from methane pyrolysis was collected on the top of the molten salt. After the melt was cooled, the resultant solid contained both carbon and salt residue. The carbon was washed in warm water (80 °C), and the solid carbon was recovered by filtration. The washing-filtering process was repeated 10 times. The final solid carbon cake was dried at 100 °C for 24 h.

2.4. Characterization of Quenched Salt and Carbon Product. X-ray diffraction (XRD) measurements were made on a Panalytical Empyrean diffractometer with copper Kα source to examine the crystalline structure of the quenched solid salt and carbon product. The reflection angle, 2θ, was varied from 10 to 90°. Raman spectra of solid carbon product were collected using a LabRAM Aramis (Horiba Jobin Yvon) with a 633 nm laser. Raman spectra of the quenched molten salt samples were collected using a Horiba Jobin Yvon T64000 open-frame confocal microscope with a 488 nm laser. Quenched molten samples were sealed between two glass slides in order to load them into the spectrometer without further exposure to air. Scanning electron microscopy (SEM) was performed using an FEI XL30 Sirion FEG Digital Scanning Electron Microscope. Elemental mapping was carried out with an energy dispersive X-ray spectrometer (EDX) operated at 20 keV. Transmission electron microscopy (TEM) was conducted using a FEI Titan 80−300 TEM.

3. RESULTS AND DISCUSSION

3.1. Activity and Stability of Iron-Containing Molten Salt for Methane Pyrolysis. The methane conversions as a function of temperature (700 to 1050 °C) in bubble columns containing different mixtures of molten Fe/NaKCl are shown in Figure 2a. In the absence of iron chloride, the methane conversion of the eutectic NaKCl is low and similar to pure KCl which is relatively inactive.[33] Conversion in these unreactive salts is attributed to gas-phase reactions inside the bubble. With the addition of iron(III) chloride into NaKCl, the conversion increases significantly as the concentration increases from 1 to 3 wt % of Fe in the NaKCl host salt. The conversion does not continue to increase further when additional iron salt is added beyond 3 wt % Fe. We suspect that this is due to saturation of the stable soluble iron species discussed below.

Methane conversions with different flow rates were measured in Fe(3%)/NaKCl and NaKCl melts at 1000 °C (Figure S3). Methane conversion decreases with increasing flow rates from 5 to 20 sccm as the reaction time in the growing bubble is long compared with the reaction during the bubble rise time. At flow rates at and above 20 sccm (the value used for our kinetics measurement), the conversion is independent of flow rate reflecting the time of bubble growth is fast compared with the rise time.

Arrhenius plots constructed using the differential methane conversions are shown in Figure 2b. The reaction kinetic parameters are determined for the different iron concentrations in the Fe/NaKCl melts and listed in Table 1. While the apparent activation energy of NaKCl is relatively high, it decreases substantially with the addition of iron(III) chloride into NaKCl. However, the apparent activation energy reaches approximately a minimum at Fe(3%)/NaKCl (171 kJ/mol) and does not significantly decrease further as the amount of iron in NaKCl is increased. The apparent activation energy for pyrolysis on Fe(3%)/NaKCl is compared with that of the previously reported solid[41−44] and molten catalysts in Table 2.

Table 1. Reaction Kinetic Parameters of Fe/NaKCl's for Methane Pyrolysis

Fe (wt %)	apparent activity energy (kJ/mol)	pre-exponential factor (s^{-1})	rate constant at 1000 °C (s^{-1})	R^2
0	301 ± 7	6.5×10^{10}−2.8×10^{11}	0.056−0.066	0.9836
1	178 ± 5	7.0×10^{5}−2.0×10^{6}	0.055−0.062	0.9779
3	171 ± 5	5.7×10^{5}−1.8×10^{6}	0.088−0.099	0.9620
5	171 ± 5	6.3×10^{5}−1.7×10^{6}	0.097−0.102	0.9718
7	167 ± 8	1.2×10^{5}−6.2×10^{5}	0.105−0.120	0.9852

Table 2. Catalytic Activities of Different Catalysts

samples	apparent activity energy (kJ/mol)	catalysts
Fe(3%)/NaKCl	171 ± 5	molten salt
molten $MnCl_2$(50)-KCl(50)[33]	153 ± 16	molten salt
molten Ni(27)−Bi(73)[29]	208	molten alloy
molten Bi[29]	310	molten alloy
gas phase[41]	422	noncatalytic reaction
Ni/SiO_2[42]	96.1	solid
activated carbon[43]	200	solid
carbon black[44]	172−222	solid

Among molten catalysts that have been reported to produce separable carbon products, Fe(3%)/NaKCl has the second lowest apparent activation energy, and it approaches that of solid catalysts.

When iron is added to NaKCl, the pre-exponential factor of the apparent first-order rate constant sharply decreases together with the apparent activation energy. This observation is consistent with the high gas-phase collision rate (pre-exponential) of the uncatalyzed, gas-phase, reaction in the inactive NaKCl where the transition state energy barrier is high, changing in the presence of a catalytic iron species at the gas−liquid interface. When the iron is present, the apparent activation energy is reduced; however, because the salt surface area offers only limited access to reactive sites, the pre-exponential is much smaller and partially compensates for the decrease in the apparent activation energy (Table 1). The gas-surface collision frequency for the molten salt (liquid) is much lower than the gas-phase collision frequency. As the major reaction pathway shifts from the high collision frequency, high barrier, gas phase for NaKCl, to the lower collision frequency, lower barrier, active liquid surface for Fe/NaKCl, the pre-exponential factor of the melt decreases due to the decreased collision rate with the liquid surface compared with the high gas-phase collision rate.

From the comparison of activities of different iron-containing molten salts, it can be surmised that the active sites for methane pyrolysis with the apparent activation energy of approximately 171 kJ/mol are formed when iron chloride is added to the NaKCl. Increasing Fe to approximately 3 wt % iron gives rise to increasing activity; however, further increases in Fe do not give rise to further increases in activity. We suspect that only in relatively dilute mixtures are the iron(III) species stabilized against reduction by surrounding alkali halides and that above 3 wt % the iron can be reduced and

https://dx.doi.org/10.1021/acscatal.0c01262
ACS Catal. 2020, 10, 7032−7042

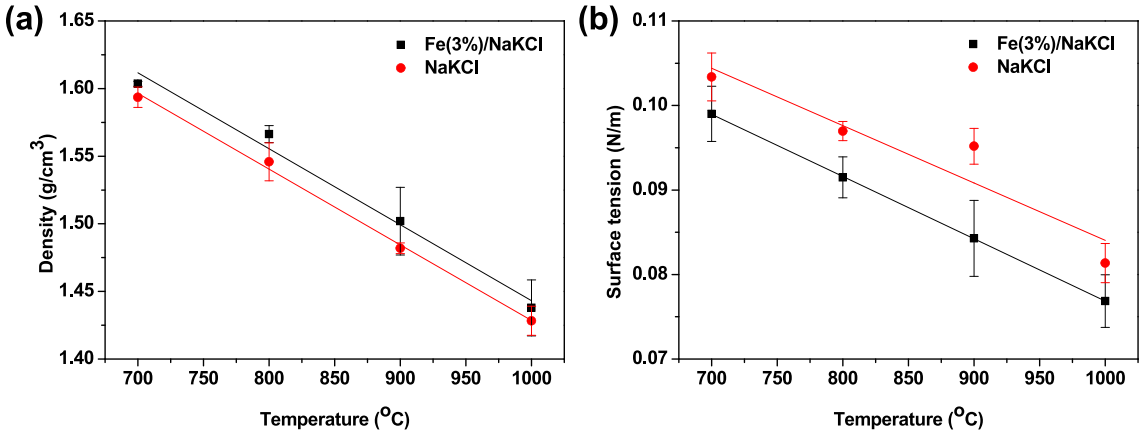

Figure 3. Density (a) and surface tension (b) of NaKCl and Fe(3%)/NaKCl molten salt mixtures versus temperature.

would likely aggregate into larger insoluble metallic iron particles.

Previous work has established the presence of stable iron (II or III) chloride in NaKCl melts at elevated temperatures under reducing conditions. The reduction reaction of iron chloride into Fe^0 is reversible and diffusion controlled.[39] HCl could be produced when iron chloride is reduced by hydrogen or methane in a bubble column. The produced HCl is possibly dissolved in the melt mixture and stabilized as $HCl + FeCl_3 \rightarrow H^+(FeCl_4)^-$ or it can react with Fe^0 to produce iron chloride again. The stability of the iron chloride is increased by forming the $(FeCl_4)^-$ tetrahedrally coordinated anionic complex in the NaKCl.[37,38] In the case of Fe(3%)/NaKCl, although a fraction of the iron chloride may be reduced to Fe^0, there will always be iron(III) chloride present even in a reducing environment (e.g., with hydrogen and methane). The presence of stable iron chloride in the melt is discussed further below.

In order to confirm the presence of a solubilized iron compound, hydrodynamic parameters (i.e., density and surface tension) were measured for the neat NaKCl melt and a 3 wt % $FeCl_3$/NaKCl melt (post reduction in 5% H_2 in Ar at 700 °C) as a function of temperature (Figure 3). The density of the Fe(3%)/NaKCl is minimally greater than the neat salt (Figure 3a). This small increase is expected, as iron-containing compounds (e.g., Fe(0), $FeCl_2$, and $FeCl_3$) have a markedly higher density than NaKCl, but are only present in a small quantity (i.e., 3 wt %).

The surface tension of the Fe(3%)/NaKCl is ∼5% lower than the neat salt at all temperatures (Figure 3b). The lowering of the surface tension suggests both that (1) a new compound has formed upon the addition and partial reduction of $FeCl_3$ in NaKCl; and (2) that new compound is present at the gas−liquid interface. Point (2) is particularly important when considering the catalytic capabilities of high-temperature liquids, because reactant gases only interact with the surface liquid layers, which can differ from the bulk significantly.[30] Both iron particles and iron-containing molecular complexes are expected to preferentially segregate to the gas−liquid interface upon formation.[45−48] However, particles typically increase the surface tension,[45−47] while ionic complexes typically decrease the surface tension.[48] Therefore, the lowering of the surface tension observed in Figure 3b suggests that the $FeCl_3$ additive has complexed with the NaKCl constituents, rather than being fully reduced to Fe(0) particles.

The activities of Fe(3%)/NaKCl and NaKCl were measured over continuous runs of 50 h at 1000 °C, Figure 4. Although

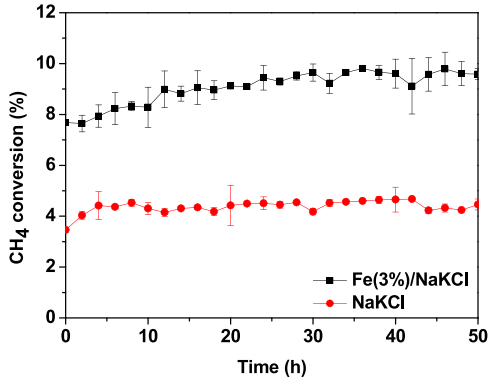

Figure 4. Methane conversion over 50 h of continuous run: reaction temperature = 1000 °C, 20 sccm of reactant gas (100 vol % of CH_4), and 50 sccm of sweep gas (100 vol % of Ar).

the complexation of $FeCl_3$ with NaKCl significantly suppressed the vapor pressure of $FeCl_3$, a small amount of solid condensate was observed on the reactor outlet at 1000 °C. However, most vaporized salt mixtures were recondensed into the melt phase by being cooled in the headspace of the bubble column reactor. In the Fe(3%)/NaKCl, mixture, the methane conversion increases from 8% to 9.5% for the first 10 h and then remains stable. In NaKCl, the methane conversion increases from 3.5% to 4.5% for the first 5 h and then stabilizes. The initial increase of the methane conversion in both cases might be attributed to the initial accumulation of solid carbon product in the melts which increases the viscosity of the melt and decreases the bubble residence time by decreasing the bubble rise velocity. After the initial period, further increases in carbon accumulate at the top of the melt effectively establishing a saturation solid carbon concentration in the melt systems. For a continuous run of 50 h, the methane conversion of Fe(3%)/NaKCl remains higher than that of NaKCl. Assuming 50% of the activity is from the 3 wt % Fe in the Fe(3%)/NaKCl salt, this represents 2.5 mol of carbon produced per mole of Fe present in the salt.

3.2. Quenched Salt Characterization. X-ray diffraction data obtained from the quenched Fe(3%)/NaKCl and NaKCl are shown in Figure 5a. Sharp diffraction peaks from NaCl and KCl are clearly observed in both quenched molten salts. Several unique broad peaks are observed in the quenched Fe(3%)/NaKCl; their intensities are relatively low compared with the NaCl and KCl peaks. Although not definitive, the

https://dx.doi.org/10.1021/acscatal.0c01262
ACS Catal. 2020, 10, 7032−7042

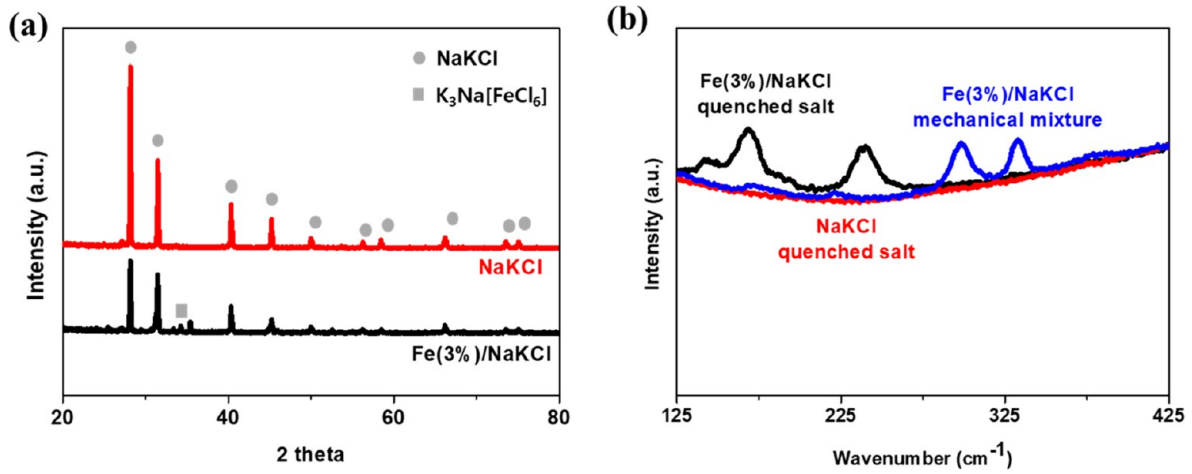

Figure 5. (a) X-ray diffraction patterns and (b) Raman spectra from samples of quenched molten salt and mechanically mixed Fe(3%)/NaKCl and NaKCl.

reflections are consistent with iron−sodium-potassium chloride complexes such as $K_3Na[FeCl_6]$. Although without in situ XRD analysis, no definitive statement can be made, and several iron ionic complexes are thought to be formed in the molten alkali chlorides.[37,38] Further, molten NaKCl is transparent and colorless, while Fe(3%)/NaKCl has a brownish color (Figure S4). The brownish color of Fe(3%)/NaKCl is consistent with the presence of an iron−sodium-potassium chloride complex or/and well-dispersed iron particles in the melt.[35] There is no XRD evidence of a reflection of metallic iron, which suggests that the amount of the metallic iron is negligible or any particles are too small to have detectable reflections.

The Raman spectrum of the solid Fe(3%)/NaKCl after rapidly quenching the molten salt (black curve, Figure 5b) has characteristic peaks at low wavenumbers (~170 cm^{-1} and ~240 cm^{-1}) in comparison to neat NaKCl (red curve, Figure 5b) and $FeCl_3$ physically mixed and ground together with NaKCl and then dried at 150 °C overnight (blue curve, Figure 5b). The neat NaKCl has no vibrational features in the region of interest, while $FeCl_3$ physically mixed has characteristic peaks at low wavenumbers (~300 cm^{-1} and ~330 cm^{-1}) with weak features at ~173 cm^{-1} and ~220 cm^{-1}. These modes may be attributed to $FeCl_3$ structures and/or iron oxides present in the raw salt. Many similar iron chloride ion derivatives are reported to have vibrational modes in the 100−350 cm^{-1} range.[49,50] For examples, 148 and 331 cm^{-1} for $NaFeCl_4$ and 141, 159, and 339 cm^{-1} for $KFeCl_4$,[49] in these mixtures the tetrahedrally coordinated $(FeCl_4)^-$ complex is thought to be stabilized.[40] Octahedrally coordinated $(FeCl_6)^{3-}$ has been observed in $Cs_2NaFeCl_6$ with a shift to lower frequency in the primary symmetric stretching frequency from approximately 332 cm^{-1} to 294 cm^{-1}.[40] There have been no prior studies with mixtures of the eutectic alkali halide with Fe(III) chloride, and it is not possible at this point to make specific peak assignments with confidence. Nonetheless, by comparison with assignments for the $(FeCl_4)^-$ in $Cs_2NaFeCl_6$, we can tentatively suggest the 170 and 240 cm^{-1} vibrations may represent breathing modes of the octahedral $(FeCl_6)^{3-}$ which forms upon cooling as the 4-fold coordination of $(FeCl_4)^-$ present in the dilute melt converts to the 6-fold coordination of the solid $(FeCl_6)^{3-}$.[40] In the eutectic NaClKCl mixture, it is not surprising that the vibrational spectra are different from those obtained from previously studied mixtures. Comparing Raman spectra from the flash-frozen Fe(3%)/NaKCl sample and the mechanical mixture of $FeCl_3$ with NaKCl shows no shared vibrational bands and supports the existence of distinct molecular ion complexes formed in mixtures of $FeCl_3$ with KCl and NaCl upon melting and reducing with 5% hydrogen.

The product selectivities for methane pyrolysis were measured at 1000 °C in both Fe(3%)/NaKCl and NaKCl. During the selectivity measurement using a residual gas analyzer mass spectrometer, the methane conversion was set to 4% in both melts by adjusting the bubble residence time. While NaKCl shows 89.2% hydrogen selectivity with 8.9% C_2 and 1.9% C_{6+} hydrocarbon selectivities, an increased 92.4% hydrogen selectivity is observed with 6.7% C_2 and 0.9% C_{6+} hydrocarbon selectivities in Fe(3%)/NaKCl.

The composition of deuterated products from the H−D exchange in mixture of CH_4 and D_2 was analyzed at different temperatures (Figure 6). The molar ratio of D_2 and CH_4 was

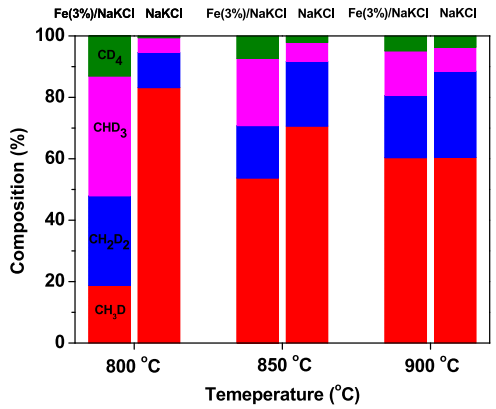

Figure 6. Composition of deuterated methane products from H−D exchange: 20 sccm of CH_4-D_2 mixture gas (CH_4:D_2 = 20:80 vol %) and 30 sccm of sweep gas (100 vol % of Ar).

kept at 4 with the total flow rate of 20 sccm. The overall methane conversions are adjusted to 10% at 800 °C, 20% at 850 °C, and 50% at 900 °C in both Fe(3%)/NaKCl and NaKCl melts by adjusting the bubble residence time. At a relatively low temperature (i.e., 800 °C), CHD_3 is the major deuterated product in Fe(3%)/NaKCl, while the composition

https://dx.doi.org/10.1021/acscatal.0c01262
ACS Catal. 2020, 10, 7032−7042

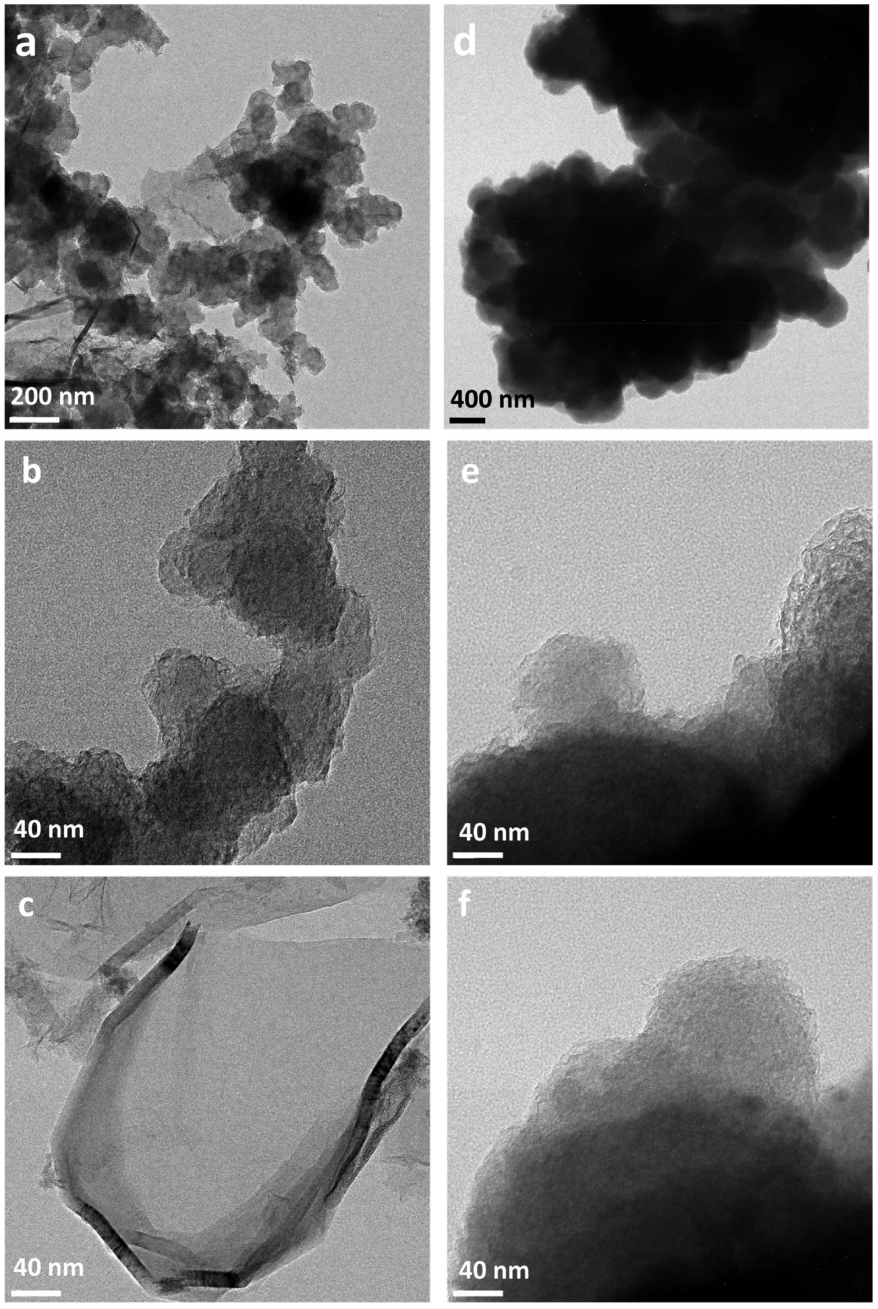

Figure 7. TEM images of carbon produced from Fe(3%)/NaKCl (a–c) and NaKCl (d–f).

of deuterated products in NaKCl follows the sequential dehydrogenation expected in the absence of any catalyst (CH_3D > CH_2D_2 > CHD_3 > CD_4).[51] At temperatures >850 °C, the noncatalytic gas-phase D–H exchange becomes dominant compared with the catalytic gas-surface D–H exchange, and the CH_3D concentration increases in Fe(3%)/NaKCl. However, the concentration of CHD_3 produced in Fe(3%)/NaKCl is still higher than that from NaKCl. It has been reported that methane is fully dehydrogenated on metallic iron surfaces,[16] resulting in CD_4 as being the major product in H–D exchange between CH_4 and D_2. The fact that the composition of deuterated products in Fe(3%)/NaKCl is different from what one expects to see in the gas phase or on solid iron surfaces implies that there is a distinct reaction mechanism in the Fe(3%)/NaKCl system. When considering the presence of iron–sodium–potassium chloride complexes in the melt, it is likely that methane is further dehydrogenated to CH or CH_2 in association with iron–sodium–potassium chloride complexes, but not fully dehydrogenated. The CH or CH_2 moieties may be oligomerized to increase the hydrogen selectivity and create the crystalline carbon structure further discussed below. In contrast, CH_3 radical is mainly formed in NaKCl, then C_{2+} hydrocarbons are formed from noncatalytic gas-phase reactions.

3.3. Characterization of Solid Carbon. Scanning electron micrographs showing the morphology of the carbon product collected from a 50 h continuous run in Fe(3%)/NaKCl after washing are shown in Figure S5a and b. There are two different solid carbon structures observed: (1) sheet-like structures (Figure S5a) and (2) ball-like structures (Figure S5b). This is because of two different reaction mechanisms in Fe(3%)/NaKCl at 1000 °C: catalytic methane pyrolysis on

https://dx.doi.org/10.1021/acscatal.0c01262
ACS Catal. 2020, 10, 7032–7042

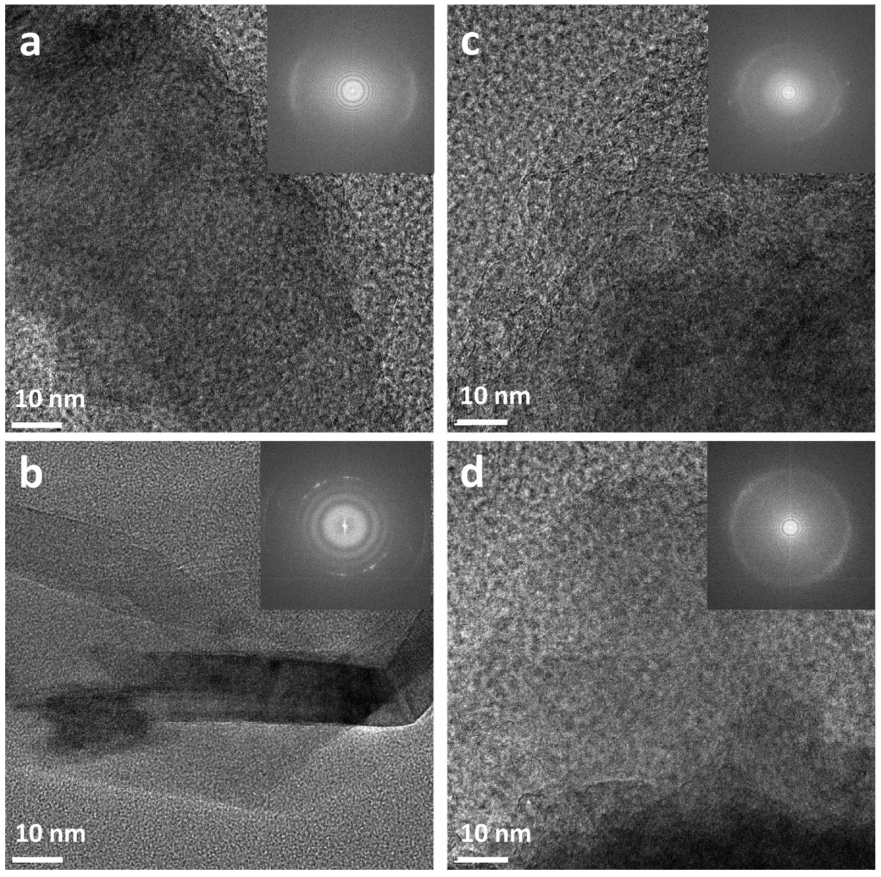

Figure 8. HRTEM images and diffraction rings (insets) of carbon produced from Fe(3%)/NaKCl (a and b) and NaKCl (c and d).

ionic complexes and noncatalytic gas-phase pyrolysis. In carbon obtained after 50 h of pyrolysis in NaKCl (Figure S5c), the same ball-like structures are observed; however, there are no observable regions with the sheet-like solid material.

Elemental mapping shows that an iron signal is diffusely dispersed everywhere on the carbon product. There are almost no aggregated iron particles identifiable in Figure S5a,b, suggesting that the major active species for methane pyrolysis in Fe(3%)/NaKCl are not associated with aggregated iron particles.

TEM images of carbon produced from Fe(3%)/NaKCl and NaKCl are compared in Figure 7. As in the SEM images (Figure S5), the morphology of carbon collected from Fe(3%)/NaKCl (Figure 7a) has two different structures: ball-like carbon (Figure 7b) and sheet-like carbon (Figure 7c). Also consistent with the SEM, TEM images of carbon produced from NaKCl show only the ball-like structures (Figure 7d–f). The electron diffraction patterns of the two different carbon structures produced in the Fe(3%)/NaKCl are shown in Figure 8. Multiple diffraction rings with polycrystalline structure are observed in the sheet-like carbon product, consistent with a graphitic structured carbon (Figure 8b). A diffraction pattern with delocalized rings consistent with amorphous carbon was obtained from the ball-like structures (Figure 8a), which matched that obtained from carbon produced in the NaKCl melt (Figure 8c,d).

High-angle annular dark field scanning TEM (HAADF-STEM) images of carbon produced from Fe(3%)/NaKCl are shown in Figure S6. Few aggregated iron particles whose sizes are larger than 100 nm are observed in Figure S6a,b, but they are fully encapsulated by carbon product and would likely be inactive. Any solid iron particles present from reduction might be initially active; however, they would deactivate quickly as they were encapsulated with carbon. Further, iron nanoparticles are known to grow carbon nanofibers from methane—none were observed. The observed trace numbers of large iron particles are not thought to be responsible for the high and long-term catalytic activity of Fe(3%)/NaKCl. Bright features are present along the edge of the sheet-like carbon (Figure S6c). These electron dense objects could come from iron–sodium–potassium chloride complexes and be responsible for the formation of graphitic sheet-like carbon. Even in a mixed amorphous–crystalline structure of the carbon product (Figure S6d), the bright signal is stronger along the small graphitic layer than is observed from the amorphous structure.

The average crystallinity of carbon produced from Fe(3%)/NaKCl and NaKCl was measured with Raman (Figure S7) and XRD (Figure S8). In the Raman spectra, the D (1350 cm^{-1}) and G (1585 cm^{-1}) bands are attributed to defected carbon and an sp^2 carbon crystalline network, respectively.[52] A relatively small intensity ratio of the D and G bands, $I(D)/I(G)$, indicates a greater degree of graphitization in the carbon. The observed $I(D)/I(G)$ ratio of the carbon product from the NaKCl is approximately 1.53, consistent with an amorphous structure, while carbon produced in Fe(3%)/NaKCl had a $I(D)/I(G)$ of approximately 0.53 indicative of a highly graphitic structure. The X-ray diffraction spectra from the carbon produced in Fe(3%)/NaKCl contained a sharp graphite peak, in further support of a reaction pathway

https://dx.doi.org/10.1021/acscatal.0c01262
ACS Catal. 2020, 10, 7032–7042

generating crystalline carbon. No such graphite diffraction peak was observed from the carbon product of pyrolysis in NaKCl.

The elemental composition of the carbon produced from Fe(3%)/NaKCl and NaKCl was measured with EDX (Table 3). The purity of carbon is over 90 atomic % from both salts; however, the carbon from Fe(3%)/NaKCl has detectable iron present.

Table 3. Elemental Composition of Carbon Produced from Melts after Water-Washing

reaction melt	Fe(3%)/NaKCl	NaKCl
C (at.%)	92.83 ± 2.61	93.67 ± 0.22
Na (at.%)	1.42 ± 0.62	2.31 ± 0.01
K (at.%)	1.63 ± 0.09	1.20 ± 0.07
Cl (at.%)	3.37 ± 0.69	2.82 ± 0.15
Fe (at %)[a]	0.75 ± 0.19	

[a]N.A. for NaKCl.

4. CONCLUSIONS

The addition of 3% by weight of Fe(III) chloride to the eutectic molten salt mixture NaCl-KCl increased the activity of the melt for methane pyrolysis in a bubble column. The apparent activation energy for pyrolysis decreased with increased $FeCl_3$ from 301 kJ/mol (0% Fe) to 171 kJ/mol (3% by weight Fe) while the pre-exponential of the apparent first-order rate constant decreased, consistent with a transition from a gas-phase collision-based reaction pathway to a surface mediated catalytic process. Further, the H−D exchange from mixtures of CH_4 and D_2 in Fe/NaKCl showed relatively large amounts of CHD_3 and CH_2D_2 where formed, distinct from observations in NaKCl and consistent with catalytic dissociative chemisorption of methane on active sites with methylene intermediates formed. Pyrolysis in the Fe/NaKCl melt produced a carbon with a sheet-like graphitic structure, which is distinct from the amorphous carbon produced from gas-phase methane pyrolysis and unlike carbon nanotubes that are typically formed on solid iron particles. Although iron contamination was present in the carbon, it was present primarily as diffusely distributed with the NaKCl consistent with the presence of homogeneously distributed $FeCl_3$. Methane pyrolysis in the iron-containing salt mixtures was observed to be stable for at least 50 h without deactivation. No metallic iron was observed in the rapidly cooled Fe/NaKCl melts by X-ray diffraction while reflections consistent with the presence of iron−sodium-potassium crystalline forms was observed. Raman spectroscopy supported the presence of an Fe(III) molecular ion in the solid salt. Although we do not yet have direct in situ evidence for a stable iron-containing molecular ion at reaction temperatures under reducing conditions, we speculate that such a complex is present and is responsible for the observed activity for C−H bond activation and deep dehydrogenation of methane and the formation of graphitic carbon at the liquid−gas interface.

■ ASSOCIATED CONTENT

Supporting Information

The Supporting Information is available free of charge at https://pubs.acs.org/doi/10.1021/acscatal.0c01262.

Surface tension measurements using the maximum bubbling pressure method; bubble size measurements using the periodicity of the same pressure trace; catalytic activity measurements versus flow rates; photographs of molten salts; SEM and TEM images of carbon produced from melts; and Raman spectra and XRD pattern of carbon from melts (PDF)

■ AUTHOR INFORMATION

Corresponding Author

Eric W. McFarland − *Department of Chemical Engineering, University of California, Santa Barbara, California 93106-5080, United States;* orcid.org/0000-0001-7242-509X; Email: ewmcfar@engineering.ucsb.edu

Authors

Dohyung Kang − *School of Chemical Engineering, Yeungnam University, Gyeongsan 38541, Korea*

Clarke Palmer − *Department of Chemical Engineering, University of California, Santa Barbara, California 93106-5080, United States;* orcid.org/0000-0001-7878-8318

Davide Mannini − *Department of Chemical Engineering, University of California, Santa Barbara, California 93106-5080, United States*

Nazanin Rahimi − *Department of Chemical Engineering, University of California, Santa Barbara, California 93106-5080, United States*

Michael J. Gordon − *Department of Chemical Engineering, University of California, Santa Barbara, California 93106-5080, United States;* orcid.org/0000-0003-0123-9649

Horia Metiu − *Department of Chemistry and Biochemistry, University of California, Santa Barbara, California 93106-9510, United States;* orcid.org/0000-0002-3134-4493

Complete contact information is available at: https://pubs.acs.org/10.1021/acscatal.0c01262

Author Contributions

#D.K. and C.P. contributed equally.

Notes

The authors declare no competing financial interest.

■ ACKNOWLEDGMENTS

This work was primarily supported by the Energy & Biosciences Institute through the EBI-Shell program and the U.S. Department of Energy, Office of Science Basic Energy Sciences, grant no. DE-FG03-89ER14048. We acknowledge the use of facilities supported by the California NanoSystems Institute and the Materials Research Science and Engineering Center (MRSEC) at UC Santa Barbara through NSF DMR 1720256 and NSF CNS 1725797.

■ REFERENCES

(1) Holladay, J. D.; Hu, J.; King, D. L.; Wang, Y. An Overview of Hydrogen Production Technologies. *Catal. Today* **2009**, *139* (4), 244−260.

(2) Midilli, A.; Ay, M.; Dincer, I.; Rosen, M. A. On Hydrogen and Hydrogen Energy Strategies II: Future Projections Affecting Global Stability and Unrest. *Renewable Sustainable Energy Rev.* **2005**, *9* (3), 273−287.

(3) Midilli, A.; Ay, M.; Dincer, I.; Rosen, M. A. On Hydrogen and Hydrogen Energy Strategies I: Current Status and Needs. *Renewable Sustainable Energy Rev.* **2005**, *9* (3), 255−271.

(4) Muradov, N. Low to Near-zero CO_2 Production of Hydrogen from Fossil Fuels: Status and Perspectives. *Int. J. Hydrogen Energy* **2017**, *42* (20), 14058−14088.

(5) Keipi, T.; Tolvanen, H.; Konttinen, J. Economic Analysis of Hydrogen Production by Methane Thermal Decomposition: Comparison to Competing Technologies. *Energy Convers. Manage.* **2018**, *159*, 264−273.
(6) Zhang, X.; Kätelhön, A.; Sorda, G.; Helmin, M.; Rose, M.; Bardow, A.; Madlener, R.; Palkovits, R.; Mitsos, A. CO_2 Mitigation Costs of Catalytic Methane Decomposition. *Energy* **2018**, *151*, 826−838.
(7) Parkinson, B.; Balcombe, P.; Speirs, J. F.; Hawkes, A. D.; Hellgardt, K. Levelized Cost of CO_2 Mitigation from Hydrogen Production Routes. *Energy Environ. Sci.* **2019**, *12*, 19−40.
(8) Chen, C. J.; Back, M. H.; Back, R. A. The Thermal Decomposition of Methane. I. Kinetics of the Primary Decompositionto C_2H_6 + H_2; Rate Constant for the Homogeneous Unimolecular Dissociation of Methane and its Pressure Dependence. *Can. J. Chem.* **1975**, *53* (23), 3580−3590.
(9) Chen, C. J.; Back, M. H.; Back, R. A. The Thermal Decomposition of Methane. II. Secondary Reactions, Autocatalysis and Carbon Formation; Non-Arrhenius Behaviour in The Reaction of CH_3 with Ethane. *Can. J. Chem.* **1976**, *54* (20), 3175−3184.
(10) Billaud, F.; Gueret, C.; Weill, J. Thermal Decomposition of Pure Methane at 1263 K. Experiments and Mechanistic Modeling. *Thermochim. Acta* **1992**, *211*, 303−322.
(11) Abanades, S.; Flamant, G. Solar Hydrogen Production from the Thermal Splitting of Methane in a High Temperature Solar Chemical Reactor. *Sol. Energy* **2006**, *80* (10), 1321−1332.
(12) Holmen, A.; Olsvik, O.; Rokstad, O. A. Pyrolysis of Natural Gas: Chemistry and Process Concepts. *Fuel Process. Technol.* **1995**, *42* (2−3), 249−267.
(13) Olsvik, O.; Rokstad, O. A.; Holmen, A. Pyrolysis of Methane in the Presence of Hydrogen. *Chem. Eng. Technol.* **1995**, *18* (5), 349−358.
(14) Abbas, H. F.; Wan Daud, W. M. A. Hydrogen Production by Methane Decomposition: A Review. *Int. J. Hydrogen Energy* **2010**, *35* (3), 1160−1190.
(15) Amin, A. M.; Croiset, E.; Epling, W. Review of Methane Catalytic Cracking for Hydrogen Production. *Int. J. Hydrogen Energy* **2011**, *36* (4), 2904−2935.
(16) Li, Y.; Li, D.; Wang, G. Methane Decomposition to CO_x-free Hydrogen and Nano-carbon Material on Group 8−10 Base Metal Catalysts: A Review. *Catal. Today* **2011**, *162* (1), 1−48.
(17) Ashik, U. P. M.; Wan Daud, W. M. A.; Abbas, H. F. Production of Greenhouse Gas Free Hydrogen by Thermocatalytic Decomposition of Methane − A Review. *Renewable Sustainable Energy Rev.* **2015**, *44*, 221−256.
(18) Otsuka, K.; Takenaka, S.; Ohtsuki, H. Production of Pure Hydrogen by Cyclic Decomposition of Methane and Oxidative Elimination of Carbon Nanofibers on Supported-Ni-based Catalysts. *Appl. Catal., A* **2004**, *273* (1−2), 113−124.
(19) Takenaka, S.; Tomikubo, Y.; Kato, E.; Otsuka, K. Sequential Production of H_2 and CO over Supported Ni Catalysts. *Fuel* **2004**, *83* (1), 47−57.
(20) Pinilla, J. L.; Suelves, I.; Utrilla, R.; Gálvez, M. E.; Lázaro, M. J.; Moliner, R. Hydrogen Production by Thermo-catalytic Decomposition of Methane: Regeneration of Active Carbons Using CO_2. *J. Power Sources* **2007**, *169* (1), 103−109.
(21) Kang, D.; Lee, J. W. Enhanced Methane Decomposition over Nickel-carbon-B_2O_3 Core-shell Catalysts Derived from Carbon Dioxide. *Appl. Catal., B* **2016**, *186*, 41−55.
(22) Steinberg, M. Fossil Fuel Decarbonization Technology for Mitigating Global Warming. *Int. J. Hydrogen Energy* **1999**, *24* (8), 771−777.
(23) Hathaway, B. J.; Davidson, J. H.; Kittelson, D. B. Solar Gasification of Biomass: Kinetics of Pyrolysis and Steam Gasification in Molten Salt. *J. Sol. Energy Eng.* **2011**, *133* (2), 021011.
(24) Adinberg, R.; Epstein, M.; Karni, J. Solar Gasification of Biomass: A Molten Salt Pyrolysis Study. *J. Sol. Energy Eng.* **2004**, *126* (3), 850−857.
(25) Geissler, T.; Plevan, M.; Abanades, A.; Heinzel, A.; Mehravaran, K.; Rathnam, R. K.; Rubbia, C.; Salmieri, D.; Stoppel, L.; Stuckrad, S.; Weisenburger, A.; Wenninger, H.; Wetzel, T. Experimental Investigation and Thermo-chemical Modeling of Methane Pyrolysis in a Liquid Metal Bubble Column Reactor with a Packed Bed. *Int. J. Hydrogen Energy* **2015**, *40* (41), 14134−14146.
(26) Plevan, M.; Geissler, T.; Abanades, A.; Mehravaran, K.; Rathnam, R. K.; Rubbia, C.; Salmieri, D.; Stoppel, L.; Stuckrad, S.; Wetzel, T. Thermal Cracking of Methane in a Liquid Metal Bubble Column Reactor: Experiments and Kinetic Analysis. *Int. J. Hydrogen Energy* **2015**, *40* (25), 8020−8033.
(27) Abanades, A.; Rathnam, R. K.; Geissler, T.; Heinzel, A.; Mehravaran, K.; Muller, G.; Plevan, M.; Rubbia, C.; Salmieri, D.; Stoppel, L.; Stuckrad, S.; Weisenburger, A.; Wenninger, H.; Wetzel, T. Development of Methane Decarbonisation Based on Liquid Metal Technology for CO_2-free Production of Hydrogen. *Int. J. Hydrogen Energy* **2016**, *41* (19), 8159−8167.
(28) Geissler, T.; Abanades, A.; Heinzel, A.; Mehravaran, K.; Muller, G.; Rathnam, R. K.; Rubbia, C.; Salmieri, D.; Stoppel, L.; Stuckrad, S.; Weisenburger, A.; Wenninger, H.; Wetzel, T. Hydrogen Production via Methane Pyrolysis in a Liquid Metal Bubble Column Reactor with a Packed Bed. *Chem. Eng. J.* **2016**, *299*, 192−200.
(29) Upham, D. C.; Agarwal, V.; Khechfe, A.; Snodgrass, Z. R.; Gordon, M. J.; Metiu, H.; McFarland, E. W. Catalytic Molten Metals for the Direct Conversion of Methane to Hydrogen and Separable Carbon. *Science* **2017**, *358* (6365), 917−921.
(30) Palmer, C.; Tarazkar, M.; Kristoffersen, H. H.; Gelinas, J.; Gordon, M. J.; McFarland, E. W.; Metiu, H. Methane Pyrolysis with a Molten Cu−Bi Alloy Catalyst. *ACS Catal.* **2019**, *9* (9), 8337−8345.
(31) Kenney, C. N. Molten-Salt Catalysis of Gas Reactions. *Catal. Rev.: Sci. Eng.* **1975**, *11* (2), 197−224.
(32) Sada, E.; Kumazawa, H.; Kudsy, M. Pyrolysis of Lignins in Molten-Salt Media. *Ind. Eng. Chem. Res.* **1992**, *31* (2), 612−616.
(33) Kang, D.; Rahimi, N.; Gordon, M. J.; Metiu, H.; McFarland, E. W. Catalytic Methane Pyrolysis in Molten $MnCl_2$-KCl. *Appl. Catal., B* **2019**, *254*, 659−666.
(34) Rahimi, N.; Kang, D.; Gelinas, J.; Menon, A.; Gordon, M. J.; Metiu, H.; McFarland, E. W. Solid Carbon Production and Recovery from High Temperature Methane Pyrolysis in Bubble Columns Containing Molten Metals and Molten Salts. *Carbon* **2019**, *151*, 181−191.
(35) Zhang, H.; Dasbiswas, K.; Ludwig, N. B.; Han, G.; Lee, B.; Vaikuntanathan, S.; Talapin, D. V. Stable Colloids in Molten Inorganic Salts. *Nature* **2017**, *542*, 328.
(36) Busey, R. H.; Giauque, W. F. The Equilibrium Reaction $NiCl_2$ + H_2 = Ni + 2HCl. Ferromagnetism and the Third Law of Thermodynamics1. *J. Am. Chem. Soc.* **1953**, *75* (8), 1791−1794.
(37) Lewis, G. K.; Drickamer, H. G. High-pressure Mossbauer Resonance Studies of the Conversion of Fe(III) to Fe(II) in Ferraic Halides. *Proc. Natl. Acad. Sci. U. S. A.* **1968**, *61* (2), 414−421.
(38) Khalaghi, B.; Kvalheim, E.; Tokushige, M.; Teng, L.; Seetharaman, S.; Haarberg, G. M. Electrochemical Behaviour of Dissolved Iron Chloride in KCl+LiCl+NaCl Melt at 550°C. *ECS Trans.* **2014**, *64* (4), 301−310.
(39) Haarberg, G. M.; Keppert, M. Diffusion Kinetics for the Electrochemical Reduction of Fe (III) Species in Molten NaCl-$FeCl_3$. *ECS Trans.* **2008**, *16* (49), 309−315.
(40) Voyiatzis, G. A.; Kalampounias, A. G.; Papatheodorou, G. N. The Structure of Molten Mixtures of Iron(III) Chloride with Caesium Chloride. *Phys. Chem. Chem. Phys.* **1999**, *1* (20), 4797−4803.
(41) Keipi, T.; Tolvanen, K. E. S.; Tolvanen, H.; Konttinen, J. Thermo-catalytic Decomposition of Methane: The Effect of Reaction Parameters on Process Design and the Utilization Possibilities of the Produced Carbon. *Energy Convers. Manage.* **2016**, *126*, 923−934.
(42) Gilliland, E. R.; Harriott, P. Reactivity of Deposited Carbon. *Ind. Eng. Chem.* **1954**, *46* (10), 2195−2202.
(43) Kim, M. H.; Lee, E. K.; Jun, J. H.; Kong, S. J.; Han, G. Y.; Lee, B. K.; Lee, T.-J.; Yoon, K. J. Hydrogen Production by Catalytic

Decomposition of Methane over Activated Carbons: Kinetic Study. *Int. J. Hydrogen Energy* **2004**, *29* (2), 187−193.
(44) Lee, E. K.; Lee, S. Y.; Han, G. Y.; Lee, B. K.; Lee, T.-J.; Jun, J. H.; Yoon, K. J. Catalytic Decomposition of Methane over Carbon Blacks for CO_2-free Hydrogen Production. *Carbon* **2004**, *42* (12), 2641−2648.
(45) Harikrishnan, A. R.; Dhar, P.; Agnihotri, P. K.; Gedupudi, S.; Das, S. K. Effects of Interplay of Nanoparticles, Surfactants and Base Fluid on the Surface Tension of Nanocolloids. *Eur. Phys. J. E: Soft Matter Biol. Phys.* **2017**, *40* (5), 53.
(46) Bhuiyan, M. H. U.; Saidur, R.; Amalina, M. A.; Mostafizur, R. M.; Islam, A. Effect of Nanoparticles Concentration and Their Sizes on Surface Tension of Nanofluids. *Procedia Eng.* **2015**, *105*, 431−437.
(47) Tanvir, S.; Qiao, L. Surface Tension of Nanofluid-type Fuels Containing Suspended Nanomaterials. *Nanoscale Res. Lett.* **2012**, *7* (1), 226.
(48) Boardman, N. K.; Palmer, A. R.; Heymann, E. The Constitution of Ionic Liquids. Part 3.—The Surface Tensions of Molten Salts and Their Mixtures. *Trans. Faraday Soc.* **1955**, *51* (0), 277−286.
(49) Palvadeau, P.; Cerisier, J.; Guillot, C.; Venien, J. P.; Rzepka, E.; Lefrant, S. Vibrational Spectra and Force Constants of the Alkali Tetrahalogenoferrates $MFeCl_4$ (M = Li, Na, K, Rb, Cs). *Solid State Commun.* **1990**, *75* (5), 383−387.
(50) Papatheodorou, G. N.; Voyiatzis, G. A. Vibrational Modes and Structure of Molten Iron(III) Chloride. *Chem. Phys. Lett.* **1999**, *303* (1), 151−156.
(51) Pratt, G.; Rogers, D. Homogeneous Isotope Exchange-Reactions. Part 2.-CH_4/D_2. *J. Chem. Soc., Faraday Trans. 1* **1976**, *72*, 2769−2776.
(52) Pimenta, M. A.; Dresselhaus, G.; Dresselhaus, M. S.; Cancado, L. G.; Jorio, A.; Saito, R. Studying Disorder in Graphite-based Systems by Raman Spectroscopy. *Phys. Chem. Chem. Phys.* **2007**, *9* (11), 1276−1291.

https://dx.doi.org/10.1021/acscatal.0c01262
ACS Catal. 2020, 10, 7032−7042